Geophysical Journal International

Geophys. J. Int. (2019) **216,** 676–691
Advance Access publication 2018 October 25
GJI Gravity, geodesy and tides

doi: 10.1093/gji/ggy443

Modelling the elevation-dependent seasonal amplitude of tropospheric delays in GPS time-series using DInSAR and meteorological data

H. Samadi Alinia[1], K.F. Tiampo,[2] S.V. Samsonov[3] and P.J. González[4]

[1]*Department of Earth Sciences, Faculty of Science, Western University,1151 Richmond Street, London, Ontario, Canada, N6A 3K7. E-mail: alinia_202000@yahoo.com*
[2]*Department of Geological Sciences, Earth Science and Observation Center, University of Colorado Boulder, Boulder, CO 80309, USA*
[3]*Natural Resources Canada, Ottawa, Ontario, Canada*
[4]*University of Liverpool, Dept. Earth, Ocean and Envirnoment, United Kingdom*

Accepted 2018 October 24. Received 2018 October 16; in original form 2017 September 04

SUMMARY

A dominant source of error in space-based geodesy is the tropospheric delay, which results in excess path length of the signal as it passes through the neutral atmosphere. Many studies have addressed the use of global weather models and local meteorological observations to model the effects of this error in Global Positioning System (GPS) and Differential Interferometric Synthetic Aperture Radar (DInSAR) data. However, modelling of zenith tropospheric delays (ZTDs) errors in the GPS data, particularly in the areas of strong topographic relief, is highly problematic because ZTD estimates cannot be captured by low resolution weather models and often it is not possible to find a nearby weather station for every GPS station. In this paper, we use DInSAR data with high spatial and temporal resolution from the volcanic island of Hawaii to estimate the seasonal amplitudes of ZTD signals, which then are used to remove this error from GPS data. Here we observe the seasonal amplitude for more than one million DInSAR pixels for the time period between 2014 and 2017 and propose a best-fitting elevation-dependent model. This model is an integration of the exponential refractivity function and is linked to the observations from a radiosonde station and a weather station. It estimates seasonal amplitudes ranging from 0.2 cm at the highest elevations to 5.6 cm at the lower elevations, increasing exponentially from the DInSAR reference elevation. To demonstrate the potential of this model for correction of GPS data, we compare the modelled seasonal amplitude to the observed seasonal amplitudes of the variation of the local ZTD, computed from the Canadian Spatial Reference System-precise point positioning (CSRS-PPP) online application, for 21 GPS stations distributed throughout the island. Our results show that this model provides results with root-mean-square error (rmse) values of less than 1 cm for the majority of GPS stations. The computed rmse of the residuals between the modelled seasonal signal and the high frequency variations of the ZTD signal at each station relative to the reference GPS station, here PUKA, range between 0.7 and 4.1 cm. These estimated values show good agreement with those computed for the rmse of the residuals computed between the observed seasonal signal and the high frequency variations of ZTD, ranging from zero to 0.3 cm. This confirms the potential of the proposed DInSAR model to accurately estimate the seasonal variation of ZTDs at GPS stations at any arbitrary altitude with respect to the reference station.

Key words: Satellite geodesy; Atmospheric effects (volcano); Time-series analysis; Radar interferometry; Image processing; Fourier analysis.

Downloaded from https://academic.oup.com/gji/article-abstract/216/1/676/5144766 by CSIC user on 11 June 2020

© The Author(s) 2018. Published by Oxford University Press on behalf of The Royal Astronomical Society.

1 INTRODUCTION

The troposphere is defined as the neutral, non-ionized layer of the atmosphere which extends from Earth's surface to an altitude of approximately 10–15 km above sea level. In the lower part of this layer, below 5 km, variations in the atmospheric parameters, including temperature, pressure and the water vapour pressure, change the refractivity of the radio signals travelling between satellites and the ground. This change in refractivity results in a delay, called the tropospheric delay, in the arrival of the signal and an increase of between 2 and 30 m in the path length of the signal (Spilker 1996; Wadge *et al.* 2002). The tropospheric delay can be divided into hydrostatic (dry), wet and liquid components (Saastamoinen 1972). The hydrostatic component, a function of the dry gases in the atmosphere, is computed from surface air pressure measurements (Mendes & Langley 1994) and causes approximately 90 per cent of the total delay (Bevis *et al.* 1994; Fotiou & Pikridas 2012). The wet component primarily depends on the water vapour pressure, which is highly variable in space and time. The liquid component has a negligible contribution, on the order of approximately mm (Hanssen 2001). Among these components, the wet component has a larger contribution to the variations of the total delays in the radio signals (Bevis *et al.* 1994; Fotiou & Pikridas 2012). The wet component of the delay is the major source of the seasonal variations in the total troposphere delay and it is highly dependent on the topography (Jin *et al.* 2007).

Knowledge of the zenith tropospheric path delay (ZTD) is important for providing information for accurate positioning as well as for monitoring of spatial and temporal weather and climate variations. Several methods have been proposed to correct the ZTD errors in Global Positioning System (GPS) measurements. In general, these methods either use meteorological instrument observations and numerical weather prediction (NWP) data from global weather forecasts such as the European Centre for Medium-Range Weather Forecasts (ECMWF) at a grid spacing of $0.125^\circ \times 0.125^\circ$ (Bevis *et al.* 1992; Van Dam *et al.* 1994; Foster *et al.* 2006; Fotiou & Pikridas 2012), or standard models that are not dependent on surface meteorological data [e.g. the Hopfield model (Hopfield 1969), the Sastamoinen model (Sastamoinen 1973) and the modified Hopfield model (Goad & Goodman 1974)]. These methods are routinely incorporated into GPS network processing (Flouzat *et al.* 2009) and precise point positioning (PPP) (Kouba & Heroux 2001; Dousa & Vaclavovic 2014), the latter of which is used in this study. According to Jin *et al.* (2007), ZTD estimates obtained from non-meteorological data are not as accurate as those obtained from meteorological data because of the strong dependency of the ZTD on the atmospheric parameters. However, the primary issue is that only a few GPS stations are collocated with a meteorological instrument that measures the weather parameters at the site (Vedel *et al.* 2001). Most recently, Lu *et al.* (2016) conducted a study providing tropospheric gradient with high temporal resolution and improvement in positioning accuracy by employing multi-GNSS processing.

Various studies that take advantage of the similar effect of the tropospheric delay on both GPS and DInSAR signals have used external data such as GPS measurements to mitigate the effect of tropospheric delays in DInSAR data (Hanssen 2001; Ge *et al.* 2003; Yu *et al.* 2017). Some researcher have incorporated a combination of meteorological observations, GPS and digital elevation models (DEM) or applied a water vapour correction model integrated with GPS (Li *et al.* 2005; Samsonov *et al.* 2007).

Foster *et al.* (2006) studied the impact of the topography of Hawaii on the atmospheric delay and removed the delay in DInSAR data using a weather model called the Mesoscale Model Version 5 (MM5, Grell *et al.* 1995) at a horizontal resolution of 3 km. The MM5 output (3-D refractivity field) can be derived within 0.5 hours of the radar acquisition time, and can forecast only 12 hr forward from the initial acquisition. They showed that for the relatively short time period between 2003 September 29 and 2003 November 03, the interferogram signals represent the atmospheric delays and are in good agreement with those predicted by the MM5 model, particularly for mountainous areas such as Mauna Loa and Mauna Kea.

Samsonov *et al.* (2014) developed an approach to remove the seasonal component of the tropospheric error from DInSAR ground deformation time-series. They used meteorological and radiosonde data observed at the stations located in the Naples Bay region of Italy and computed the refractivity at Earth's surface and at altitude, respectively. They proposed an elevation-dependent exponential model that can be used to calculate the seasonal amplitude of differenced ZTD at each DInSAR location relative to a reference location. Their model provides the best fit to the seasonal amplitudes of the troposphere observed in DInSAR-derived height time-series at elevations between 200 and 700 m above mean sea level (msl), although the fit is not as good at higher elevations. They suggest that the deviation of their model from the seasonal amplitudes at higher elevations is due to either the spatial filtering applied to the interferograms or the use of simple sine function in calculating the tropospheric amplitude, which can underestimate the seasonal cycle of troposphere signals. They demonstrated that their proposed correction model could reduce the noise in DInSAR height time-series by as much as 50 per cent (Samsonov *et al.* 2014).

Modelling of ZTD is problematic in volcanoes or mountainous areas with large topographic relief, particularly in a moist, heterogeneous tropical atmosphere like Mauna Loa, Hawaii (González *et al.* 2010). This is because there is a strong interaction between winds and high mountains influencing the pattern of local weather parameters, including water vapour pressure both horizontally and vertically (e.g. generating clouds on the windward side of the mountain and dry, clear skies on the leeward side of the mountain).

Both DInSAR and GPS microwaves are affected by the seasonal tropospheric variability in a similar way. Therefore, spatially dense DInSAR can be used for correcting spatially sparse GPS data. Motivated by the results of Samsonov *et al.* (2014), here we use DInSAR data with high spatial and temporal resolution to propose an elevation-dependent refractivity model which also is dependent on the spatial and temporal variations in the weather parameters. This model estimates the local seasonal variations of troposphere signal accurately in GPS data in the area containing the Kilauea volcano and the eastern rift zone of Mauna Loa on the island of Hawaii (Figs 1a and b). The model proposed here provides the best fit to the estimates of the amplitude of ZTDs in the vertical time-series of more than one million DInSAR pixels produced from the Multidimensional Small Baseline subset (MSBAS) technique (Samsonov & d'Oreye 2012). In the study area, we demonstrate that this model not only eliminates the need for the meteorological observations at each GPS station, but that it also can be used to accurately estimate the seasonal amplitude of local ZTD on GPS data at any altitude.

In order to evaluate the potential of the model to estimate the seasonal amplitudes of the delay in GPS data, we compare the observed and the modelled seasonal amplitude of the differenced

Downloaded from https://academic.oup.com/gji/article-abstract/216/1/676/5144766 by CSIC user on 11 June 2020

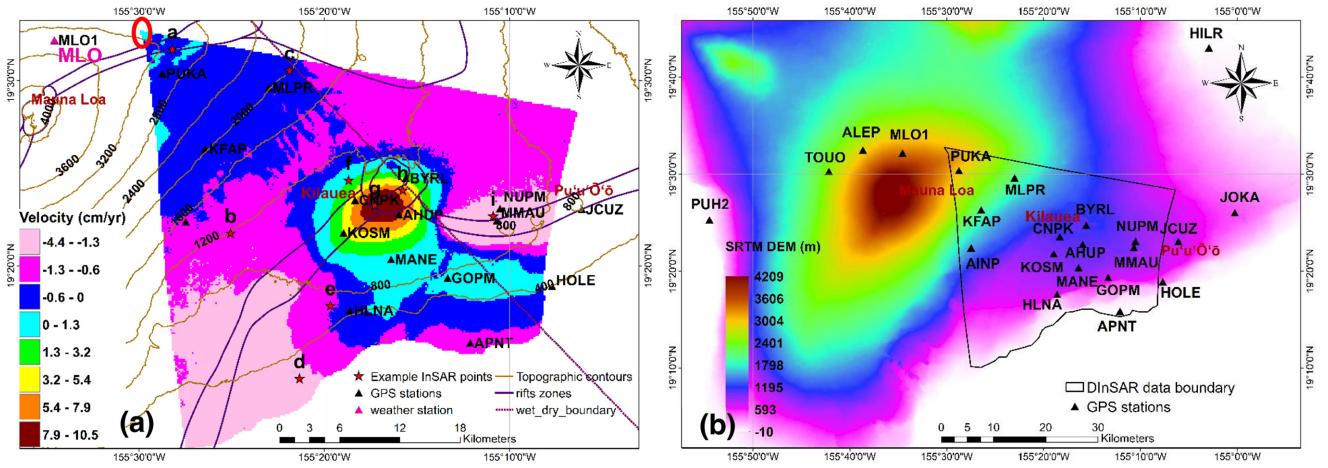

Figure 1. (a) Raster map of the deformation's velocity (in cm yr^{-1}) calculated from the linear regression on the DInSAR time-series from 2014 to 2017 at each DInSAR pixel. A positive velocity value shows uplift. Height time-series for specific DInSAR points, represented as red stars, are presented in Fig. 4. The DInSAR reference region is designated by a red circle in the NW corner (b) The SRTM-derived DEM and the distribution of the GPS stations inside and outside of the DInSAR data boundary.

ZTD at each station computed by processing the GPS data using CSRS-PPP, available from Natural Resource Canada (NRCan). Differenced ZTD is defined as the ZTD computed for the reference station subtracted from the ZTD computed for each of the other stations. In addition, we compare the root-mean-square error (rmse) of the residuals between the differenced ZTD and the modeleld seasonal signal to those computed for the residuals between the differenced ZTD and the observed seasonal signals derived from the best-fit tingsinusoidal function to each differenced ZTD for each station. The rmse of the difference between the modelled and the observed seasonal signals for every station also is computed and presented in this paper.

An overview of the geology and meteorology of our study area is provided in Section 2. In Section 3, we discuss the data and processing. In the following section, we focus on the approaches used for estimating the seasonal amplitude of the differenced ZTD, including a detailed explanation of the DInSAR height time-series fitting and the computation of the refractivity from meteorological and radiosonde measurements to derive the elevation-dependent amplitude of the differenced ZTDs. In Section 5, we elaborate on the ZTD variations computed by using CSRS-PPP and estimation of the differenced ZTD for each GPS station. Interpretation and conclusions are presented in the final section.

2 STUDY AREA

The Hawaiian volcanic island chain is located in the Pacific Ocean. The six major Hawaiian Islands include Kauai, Oahu, Molokai, Lanai, Maui and Hawaii (Big Island), stretching from northwest to southeast. Kauai is the oldest, at ∼5 Myr (millions of years), and Hawaii is the youngest at ∼0.7 Myr. These islands were formed as a result of the activity of a static mantle plume currently centred beneath Hawaii, which is composed of five main volcanoes: Mauna Loa, Kilauea, Mauna Kea, Hualalai and Kohala (Clague & Sherrod 2014). Mauna Kea, at 4207 m above msl, experienced its last eruption approximately 4000 yr ago, while Mauna Loa, at 4169 m above msl, last erupted in 1984 (Peterson & Moore 1987; Clague & Sherrod 2014; USGS 2017a).

Kilauea is located on the southeast flank of Mauna Loa and rises 1247 m above the sea level (USGS 2017b; Fig. 1b). This volcano has been erupting continuously for more than three decades at its summit and east rift zone locations. The summit crater hosts an active lava lake that has dramatic level fluctuations, dropping during deflation and rising during inflation (Wilson *et al.* 2008; USGS 2017b). This volcano has been affected by the shape of its neighbour, Mauna Loa, and has adopted a similar rift zone orientation (Fiske & Jackson 1972). However, recent research has revealed that Kilauea volcano has a separate magma plumbing system (Poland *et al.* 2012).

The climate of different regions is directly affected by the wet/windward or dry/leeward sides of volcanic islands and is strongly dependent on the shape and the heights of the volcanic peaks (Longman *et al.* 2015). The windward side of Hawaii is on the eastern slope of Mauna Kea and on the southeast flank of Mauna Loa. This region is approximately perpendicular to the direction of the northeasterly trade winds which carry moisture in the atmosphere. These prevailing trade winds make the windward side windier and wetter, which results in more rainfall per year (Zhang *et al.* 2016). As shown in Fig. 2(dashed line), we estimate the separation line between dry and wet zones based on the breakpoints proposed by Gagné & Cuddihy (1990) for Dry-Mesic and Mesic-Wet boundaries, where 2500 mm of rainfall is received at 1000 m above msl. Fig. 2 also shows a map of mean annual climate data, including air temperature, rainfall, water vapour pressure computed from the air temperature, relative humidity and air pressure. The maps of air temperature, rainfall and relative humidity are at the resolution of 250 m (Frazier 2012; Giambelluca *et al.* 2014).

The temperature map in Fig. 2(a) shows that higher elevations have lower temperatures that increase gradually toward sea level, ranging from 3.6 and 23.9 °C. The coldest zone of our study area is found symmetrically around the summit of Mauna Loa. Fig. 2(b) illustrates the average annual rainfall range from 204.1 mm to over 7629.2 mm, overlain with elevation contours. The rainfall is concentrated on the lower elevations on the east side of the Island. According to Colleen (2013), this is likely a result of the orientation of Mauna Loa volcano, parallel to the direction of the prevailing trade winds. This figure also shows that the mountain obstructs the trade winds on the leeward side of the island, resulting in less rainfall and drier conditions near the summit. As we will demonstrate

Downloaded from https://academic.oup.com/gji/article-abstract/216/1/676/5144766 by CSIC user on 11 June 2020

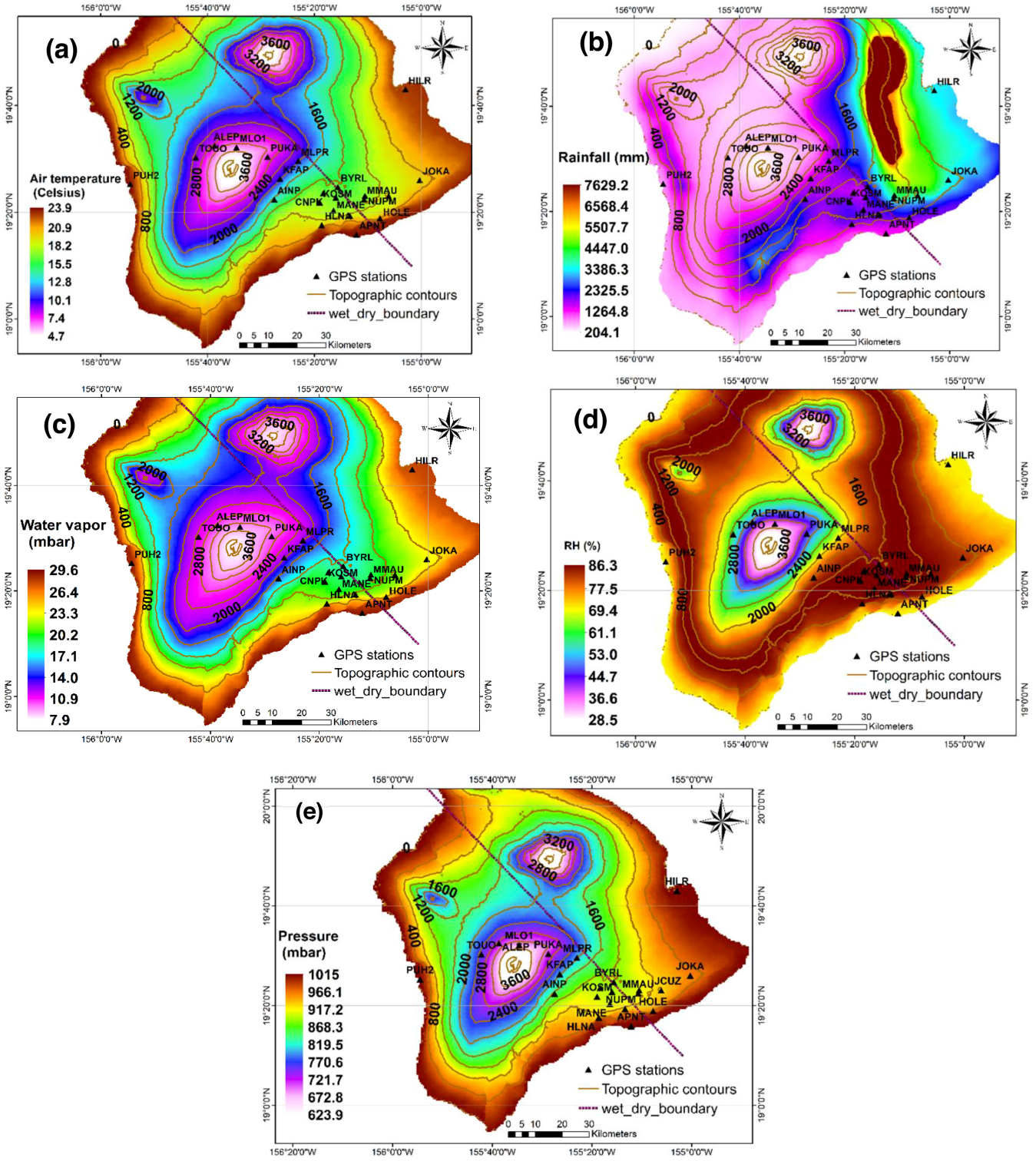

Figure 2. Mean annual climate maps including (a) air temperature, (b) rainfall, (c) water vapour computed from the air temperature (d) relative humidity. (e) Air pressure. Air temperature, rainfall and relative humidity (Frazier *et al.* 2012; Giambelluca *et al.* 2014) grids are at 250 m resolution. The brown contour lines represent elevations spaced at 400 m intervals. The windward/wet and leeward/dry side are separated with a dashed line.

later, water vapour pressure increases exponentially with temperature (Figs 2a and c). In Fig. 2(d), high relative humidity of greater than 80 per cent can be seen at lower elevations, between 400 and 1600 m above msl.

To illustrate the spatial variation of the air pressure on Hawaii, we used the following expression (Giambelluca *et al.* 2014) and applied it to the Shuttle Radar Topography Mission (SRTM)-derived DEM

Downloaded from https://academic.oup.com/gji/article-abstract/216/1/676/5144766 by CSIC user on 11 June 2020

at a resolution of 30 m.

$$P = P_0 \,/\exp\left(\frac{H}{8500}\right), \quad (1)$$

where P_0 is the pressure at msl, 1015 mbar, and H is the elevation of each pixel, in meters. As Fig. 2(e) indicates, the air pressure increases towards sea level in a symmetrical pattern around the summit of the two volcanoes.

3 DATA

For the DInSAR analysis, we collected 32 ascending Ultra-Fine 13 Wide (U13W2) images spanning from 2014 January 1 to 2017 February 2 and 34 descending Ultra-Fine 16 Wide (U16W2) images spanning between 2013 December 13 and 2017 March 3 from RADARSAT-2 satellite (Table 1). The original Ultra-Fine Wide images have a pixel spacing of 1.3 × 2.1 m (range and azimuth). During processing, these images were multilooked by a factor of 10 × 11 and then resampled to a uniform grid with the ground resolution of 30 × 30 m.

The temporal resolution of the resulting time-series is, on average, twice as dense as the RADARSAT-2 satellite revisit period of 24 d, but because some acquisitions were missed, the actual temporal resolution is slightly greater. This temporal resolution is sufficient to observe the seasonal fluctuations of the tropospheric delay. Fig. 3 presents the perpendicular baselines for U13W2 and U16W2 images.

Each SAR data set was processed independently with GAMMA software (Wegmuller & Werner 1997). A single master for each set was selected and the remaining images were resampled into the master geometry. The topographic phase was removed from the interferograms using a 30 m resolution SRTM DEM. Differential interferograms were filtered using the adaptive filtering with a filtering function based on the local fringe spectrum (Goldstein & Werner 1998) and unwrapped using the minimum cost flow algorithm (Costantini 1998). Interferogram filtering was performed with the window size of 32 pixels and an exponent, alpha, of 0.8. Because the window size is relatively small, the impact of filtering on the noise model is minimal. To extend spatial coverage to partially incoherent regions, spatial interpolation of each interferogram was performed over an eight-pixel radius for each pixel with at least eight valid pixels in its neighbourhood (equal to about 12.5 per cent). The interpolation step is very important for further time-series analysis since it is applied only to those pixels that are available on all interferograms. The time-series analysis also reduces noise that may have been introduced by the interpolation. The proposed interpolation technique has been applied in several previous studies (Samsonov *et al.* 2014, 2017, Samsonov & d'Oreye 2017). After interpolation, ascending and descending interferograms were geocoded and resampled to a common latitude/longitude grid with a uniform spatial sampling of 30 m.

The MSBAS (Samsonov & d'Oreye 2012) technique was applied to the ascending and descending data sets simultaneously to produce horizontal east–west and height time-series and annual linear deformation rates. Since the mathematical problem solved by MSBAS method is rank-deficient, regularization is introduced. This regularization acts as a low-pass filter in the temporal domain. Samsonov *et al.* (2017) demonstrated that if first- or second-order regularization methodology is used, the impact of regularization on amplitude is minimal. We used the first order regularization with the regularization parameter (λ) equal to 0.25. For a full discussion of MSBAS methodology, we refer the readers to Samsonov *et al.* (2017) and Samsonov & d'Oreye (2017). During the processing, a reference region was selected in the northwest corner, at elevation 3107 m above msl (red circle, Fig. 1a), to minimize the effect of the non-seasonal atmospheric component in the height time-series.

Fig. 1(a) shows the raster map of the surface deformation velocity computed by fitting a linear regression to the vertical component time-series of 1257000 DInSAR pixels between 2014 and 2017. The velocity values in our study area range from 4.4 cm yr^{-1} of subsidence in the eastern rift zone of Kilauea volcano, 8-km away from the volcanic cone of Pu'u'Ō'ō, to 10.5 cm yr^{-1} of uplift in the south of Kilauea volcano. As discussed above, Kilauea has been erupting continuously for more than three decades and is currently active at its summit and upper southeast rift zone.

We selected nine points over our study period, a through i, as examples of the DInSAR height time-series (Fig. 1a). The height time-series of these points before and after removal of the linear trend are presented in Fig. 4 and are labeled accordingly. Figs 4(a–c) llustrate the height time-series of points a, b and c, and show subsidence in the east rift zone of the Mauna Loa between 2014 and 2017 as a result of the massive lava outpouring from the 1984 eruption of Mauna Loa (Clague & Sherrod 2014). Figs 4(d) and (e) show subsidence of 1.4 and 0.7 cm yr^{-1}, respectively, in the outer flank of the Kilauea rift-zone (Clague & Sherrod 2014). Points f, g and h in Fig. 4 show uplift of 1.0, 10.2 and 6.4 cm yr^{-1}, respectively. This inflation between 2014 and 2017 is related to the accumulation of magma below the volcano's summit caldera and upper southwest rift zone (USGS 2017c). The vertical deformation time-series of points g and h show uplift of approximately 30 cm between 2014 and 2017 and is related to the ongoing eruption of Kilauea at the summit and at the Pu'u'ō'ō vent on the east rift zone. Deflation is observed on the upper side of east rift zone of Kilauea at location i (Fig. 4i). The vertical deformation here is related to numerous eruptions and inflation of the summit of Kilauea during this time period (Baker & Amelung 2015).

The DInSAR-derived height time-series have not been corrected for the tropospheric differential phase. These DInSAR-derived seasonal fluctuations of the differential ZTD, converted from the line-of-sight (LOS) direction by dividing it by cosine of incidence angle, can be used for correcting the ZTD error from the vertical component of the position time-series of GPS stations referenced to a local station. In order to demonstrate this analysis, the Receiver Independent Exchange Format (RINEX) data of 22 GPS stations from the Hawaii Volcano Observatory (HVO) network, 14 stations in the same region as the DInSAR data and eight stations outside of this region, were processed for the dates corresponding to the DInSAR observations. The daily RINEX files for each station are freely available on the University NAVSTAR Consortium (UNAVCO) website. These stations were selected based on the availability of the data between 2014 and 2017, incorporate a variety of elevations and wide area coverage of the study region (Fig. 1b). All these stations have observations during the same time period as the DInSAR data to ensure consistency in analysing the seasonal variations of differenced ZTD signals. Table 2 presents the information for the GPS stations, including the position of the sites, receiver types and the first and last dates of data availability. Every GPS station has data between 2014 and 2017, with the exception of station MLO1, that finished collection on 2016 August 23.

In this paper, the radiosonde data are downloaded for 2014 from the only radiosonde station available on the island, PHTO/Hilo. This station measures temperature, humidity and pressure parameters twice daily at the time of 0000 UTC and 1200 UTC at altitudes from zero to as high as 35 km. We use these observations to compute

Downloaded from https://academic.oup.com/gji/article-abstract/216/1/676/5144766 by CSIC user on 11 June 2020

Table 1. SAR datasets used in MSBAS processing: RADARSAT-2 Ultra-Fine 13 and 16 Wide (U13W2, U13W2); time span (in YYYYMMDD format), azimuth θ° measured from north clockwise and incidence φ° angles, number of available SAR images N and number of calculated interferograms M for each data set.

DInSAR set	Time span	θ°	φ°	N	M
R2-U13W2 (ASC)	2014 01 01- 2017 02 02	349	40	32	300
R2-U16W2 (DSC)	2013 12 13- 2017 03 03	191	42	34	372
Total:	2014 01 01- 2017 03 03			64	672

Note: ASC and DSC in the table stands for ascending and descending, respectively.

the refractivity over different atmospheric heights. Moreover, we employ the in situ meteorological data (pressure, temperature and relative humidity) observed between 2014 and 2017 at the closest weather station to our DInSAR reference point, MLO1, at a distance of 7.6 km. The location of MLO1 (–155.57°, 19.54°, 3395.8 m above msl) is shown in Fig. 1(a).

4 AMPLITUDE OF SEASONAL TROPOSPHERE SIGNAL

4.1 DInSAR data

The vertical seasonal fluctuation is apparent in the example height time-series of the DInSAR data presented in Fig. 4, particularly in those time-series at lower elevations, where the water vapour and temperature are at their highest amplitude (see, e.g. point d at 125 m above msl, Fig. 1a). These fluctuations, with a frequency ω, can be modelled by fitting the first harmonic of the sinusoidal function to the height time-series of each point as follow:

$$\Delta h\ (t_m) = a + b \times t_m + A\ sin\ (\omega t_m + \phi)\,. \tag{2}$$

To enhance the accuracy in determining the seasonal variations in the time-series, we first removed the linear trend term and then used a Fourier analysis. Since the data are sampled at m discrete time points, t_m, so the seasonal signal can be written as follows (Smith & Gomberg 2009):

$$A\ sin\,(\omega t_m + \phi)\ =\ C\sin(\omega t_m) + D\cos(\omega t_m)\,, \tag{3}$$

where

$$A = \sqrt{(C^2 + D^2)}\,,\ \phi\ = tan^{-1}\left(\frac{C}{D}\right),\ \omega\ =\ \frac{2\pi}{T}$$

and C and D are the frequency coefficients for annual perturbation.

We solved this function for the amplitude, A, and phase, ϕ, that maximizes the fit to the time-series data. T is the period of the signal and is extracted for every height time-series by analysing them individually in the frequency domain. A fast Fourier transform (FFT) approach was used to identify the frequency of the seasonal fluctuation in each time-series.

Fig. 5(a) presents the raster map of the observed seasonal amplitudes for all DInSAR points, overlain with the topographic maps. As this figure illustrates, the seasonal amplitude is higher at the coastal areas and lower at higher altitudes (e.g., Mauna Loa). This also can be seen in the example time-series presented in Fig. 4. As shown in Figs 4(a) and (d), we estimated amplitudes of 0.2 and 4.5 cm at altitudes of 3105 and 125 m above msl, respectively. As shown in Fig. 5(b), the estimated amplitudes increase exponentially with increasing and decreasing height from 3107 m above msl, the elevation of the reference point. Comparing the observed seasonal amplitudes with the atmospheric parameters, we can see that their spatial variations are dependent on temperature, water vapour and air pressure, again as expected, which are a function of height.

As mentioned earlier in this section, in addition to the seasonal amplitudes, the phase of the annual signals is estimated by fitting eq. (3) to each height time-series. We found values range between –180° and 180°, clockwise from north. These values correspond to the shift of the signal from the beginning of the calendar year.

Statistical analysis of the best-fitting seasonal signals to the DInSAR-derived height time-series at every pixel shows that 99 per cent of the DInSAR points have a coefficient of determination, r^2, greater than or equal to 0.2 and a p-value of less than or equal to 0.05. The scatter plot of these seasonal amplitudes with respect to the elevation indicates that they are suitable for use in deriving a model to predict the seasonal amplitudes as a function of height (Fig. 5b).

4.2 Exponential refractivity model

The speed of radio signal propagation is dependent on the material through which it travels and it is slightly lower in the atmosphere than in a vacuum. The ratio of the speed of light in a vacuum to the speed of light in the atmosphere is termed the refractive index, n, which is more conveniently expressed as the refractivity N (Bean & Dutton 1968):

$$N = 10^6\,(n-1)\,, \tag{4}$$

where N can be computed by its relationship with atmospheric parameters including pressure, temperature and water vapour pressure proposed by Smith & Weintraub (1953):

$$N = K_1\frac{P_d}{ta} + K_2\frac{e}{ta} + K_3\frac{e}{ta^2}. \tag{5}$$

In this equation, P_d is the partial pressure due to dry gases (hPa), K_i is the refractivity constants, e is the partial pressure of water vapour (hPa) and ta is the absolute air temperature (degrees Kelvin). The refractivity constants K_i were determined empirically in a laboratory. We adopt the refractivity constants computed in Rueger (2002) of 77.69 K mbar $^{-1}$, 71.29 K mbar $^{-1}$ and 375463 K^2 mbar $^{-1}$ for the refractivity constants K_1, K_2 and K_3, respectively. The partial water vapour pressure is estimated from the dew point temperature, calculated from its relationship to the relative humidity and temperature (Lawrence 2005) measured at the weather station. As proposed by Alduchov & Eskridge (1996), for dew point temperatures less than 50 °C, the partial vapour pressure can be computed as follow:

$$\mathrm{E} = 6.1037e^{17.641td/(243.27+td)}, \tag{6}$$

where td is the dew point temperature in degrees Celcius.

The tropospheric delay can be calculated through an integration of refractivity along the path of the signal in the troposphere as follows (Hopfield 1972):

$$d_{trop} = 10^{-6}\int_{path} N\mathrm{d}s. \tag{7}$$

Downloaded from https://academic.oup.com/gji/article-abstract/216/1/676/5144766 by CSIC user on 11 June 2020

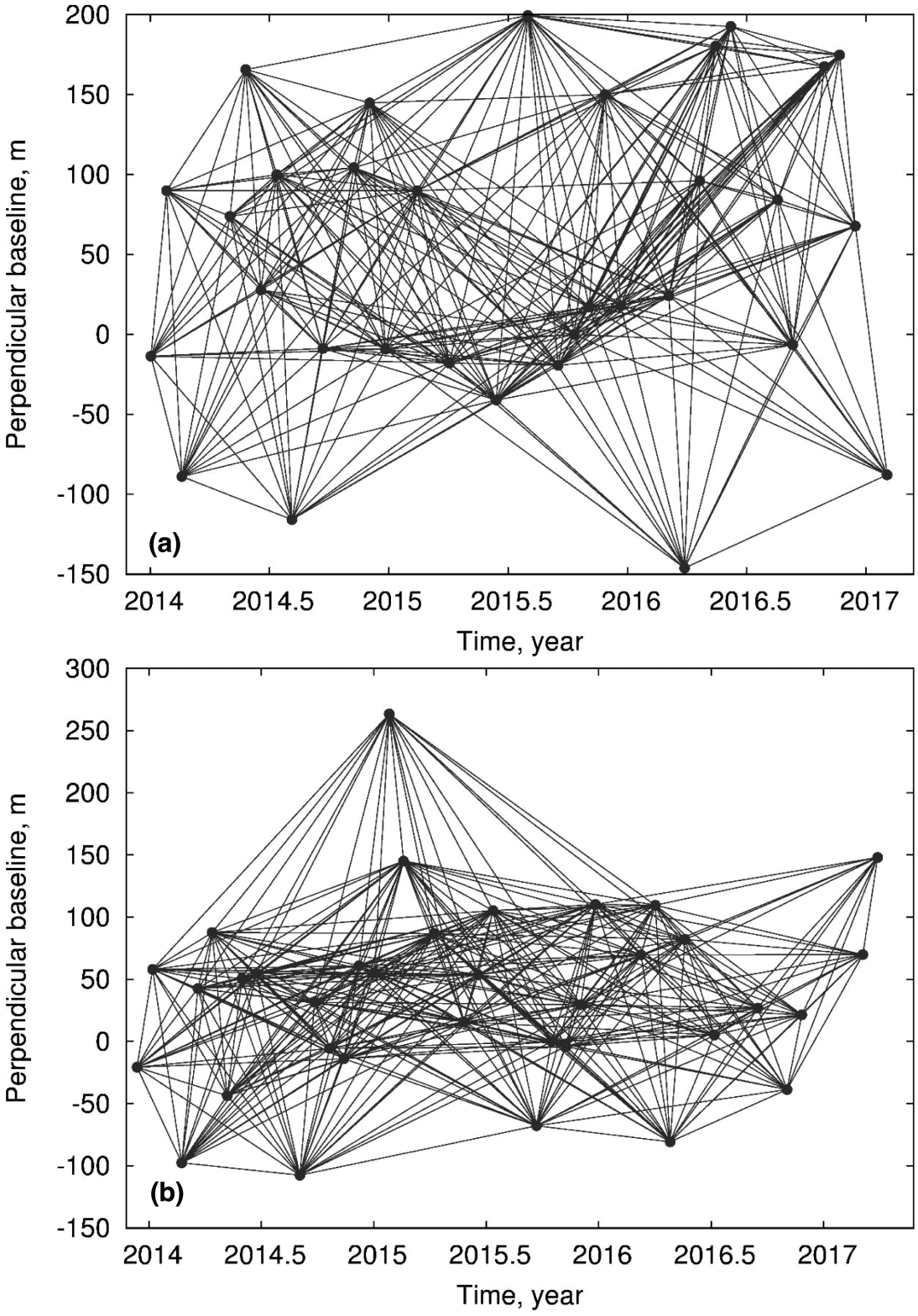

Figure 3. The perpendicular baselines as a function of acquisition dates for (a) U13W2 and (b) U16W2 images. Each dot corresponds to a SAR image and each line corresponds to an interferogram. Interferogram's spatial and temporal baselines can be read from the plot.

Downloaded from https://academic.oup.com/gji/article-abstract/216/1/676/5144766 by CSIC user on 11 June 2020

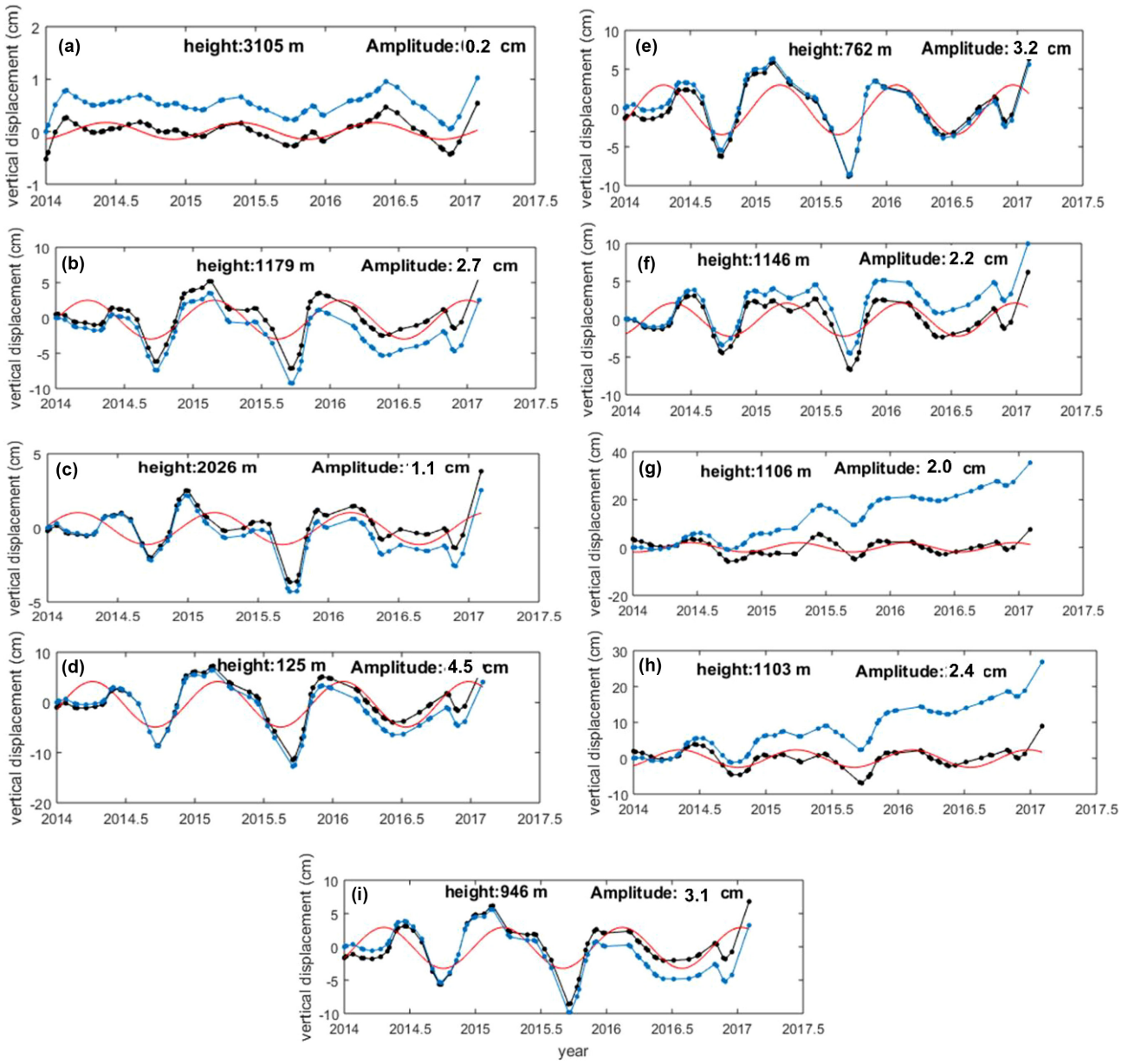

Figure 4. Example of DInSAR height time-series of the specified points *a* through *i*, shown in Fig. 1(a), before and after removal of linear regression trend and are presented in blue and black, respectively. The DInSAR acquisition dates are shown by solid circles. The modelled seasonal signals are shown in red. The height time-series of all locations are referenced to a point at elevation 3107 m above msl. In addition to the elevation of each point, the modelled seasonal amplitudes are given in each plot. Positive values indicate uplift.

The horizontal variations of N are very small compared to those in the vertical direction and it can be neglected. Taking into account the one-dimensional model and layer-by-layer exponential model for the vertical variations of refractivity proposed by Martin & Waldron (1961), the tropospheric delay in the range of elevations between any arbitrary measurement location and the reference location can be computed as follow (Samsonov *et al.* 2014):

$$\Delta d_{trop}\ (t,\ z_r, z_i) = 10^{-6}\ N_r\,(t) \int_{z_r}^{z_i} e^{-cz}\ \mathrm{d}z, \tag{8}$$

where $N_r(t)$ is the refractivity time-series computed from the temporal surface meteorological data measured at the weather station collocated with the DInSAR reference point, c is the exponential decay parameter computed from the best fitted exponential model to the refractivity values obtained from radiosonde data, z_r and z_i are the elevation of reference station and the measurement point, respectively. The elevation above sea level, in meters, is obtained from the SRTM-derived DEM.

To take advantage of the relationship between the refractivity and the tropospheric delay, we expanded eq. (8) as in Samsonov *et al.* (2014). Because we considered the reference station at a high elevation and the seasonal amplitudes increase from the elevation of the reference point, we take into account the absolute value of the resulting equation (eq. 9) to fit the model amplitudes to the observed amplitudes in DInSAR data, as appropriate.

$$amp_{ZTDi}\ (z_r, z_i) = \left| \frac{10^{-6}\,(amp_{Nr})}{ce^{cz_r}} \left(1 - e^{-c(z_i - z_r)}\right) \right|, \tag{9}$$

Downloaded from https://academic.oup.com/gji/article-abstract/216/1/676/5144766 by CSIC user on 11 June 2020

Table 2. GPS stations details.

Station	Receiver	Longitude (degree)	Latitude (degree)	Altitude (m) above msl	Start date	End date
AHUP	Trimble NetRS	-155.27	19.38	1082.9	1999 May	2017 May
ALEP	Javad TreG3th Sigma	-155.64	19.54	2895.7	2004 July	2017 May
BYRL	Trimble NetRS	-155.26	19.41	1076.7	2006 Feb.	2017 May
CNPK	Trimble NetR9	-155.31	19.39	1100.9	2008 June	2017 May
GOPM	Trimble NetRS	-155.22	19.32	739.3	1999 May	2017 May
HLNA	Trimble NetR9	-155.31	19.29	677.1	1996 Aug.	2017 May
HOLE	Trimble NetRS	-155.13	19.31	408.4	1999 May	2017 May
JCUZ	Trimble NetRS	-155.10	19.38	808.8	2007 July	2017 May
KFAP	Trimble NetRS	-155.44	19.44	2048.0	2004 July	2017 May
MLPR	Trimble NetRS	-155.38	19.49	2015.9	2005 Aug.	2017 May
NUPM	Trimble NetR9	-155.18	19.38	913.3	1999 June	2017 May
MANE	Trimble NetRS	-155.27	19.34	975.1	1999 May	2017 May
JOKA	Trimble NetRS	-155.00	19.43	466.5	2007 Oct.	2017 May
TOUO	Javad TreG3th Sigma	-155.70	19.50	2509.6	2004 July	2017 May
AINP	Trimble NetRS	-155.46	19.37	1543.1	2005 Sept.	2017 May
APNT	Trimble NetR9	-155.20	19.26	23.7	1996 Sept.	2017 May
PUH2	Trimble NetRS	-155.91	19.42	29.4	2014 March	2017 May
HILR	Trimble NetR8	-155.05	19.72	12.8	2010 May	2017 May
KOSM	Trimble NetRS	-155.32	19.36	967.7	1999 Aug.	2017 May
MLO1	Trimble NetR9	-155.58	19.54	3402.7	2004 Dec	2016 Aug
MMAU	Trimble NetRS	-155.18	19.37	929.7	2010 July	2017 May
PUKA	Trimble NetRS	-155.48	19.51	2999.8	2005 March	2017 May

where amp_{Nr} is the average seasonal amplitude of refractivity at Earth's surface, c is the decay parameter computed from radiosonde data, z_i is the elevation of the measurement points and z_r is the elevation of the reference point, 3107 m above msl. The methodologies of computing amp_{Nr} and c are described later.

In order to calculate amp_{Nr}, we initially estimated the refractivity time-series from eq. (5). We used the surface measurements for pressure, water vapour pressure and temperature observed at the in situ station MLO1 over the time span of 2014–2017 to estimate the refractivity time-series from eq. (5). The seasonal cycle in refractivity of the atmosphere is apparent in both the hourly and daily time-series shown in Fig. 6a. The amplitude of the seasonal variation, amp_{Nr}, of daily refractivity estimated from the best-fitting sinusoid function is 17.90 (N-units). This seasonal cycle is due to the seasonal variations in the climate variables, primarily due to variations in water vapour pressure and temperature, in which the maximum occurs in the summer (June) and the minimum occurs in the winter (January) of each year.

In addition, we used the data measured at the radiosonde station PHTO/HILO and computed the refractivity of the points at elevations between 0 and 35 km above the surface of Earth. We present the vertical profile of the estimates of the refractivity in Fig. 6(b). This figure illustrates the exponential decrease in the refractivity with height with a decay rate of 0.14 km^{-1}. This value is in good agreement with the empirical value given by Bean & Thayer (1959), 0.1424 km^{-1}, for elevations above 9 km. The computed parameters for the fitted exponential model are presented on the top right of this figure. This exponential model provides a good fit to the observed seasonal amplitudes of differenced ZTD in the DInSAR data, within the 90 percent confidence interval.

Examining the correlation between the observed seasonal amplitude of ZTDs and the weather variable maps illustrated in Fig. 2 shows that they are positively correlated with the variation of temperature and water vapour pressures. The estimated seasonal amplitudes are proportional to the pressure data, which it is dependent on the elevation of the points.

Using the above analysis, we can model the seasonal variations imposed by ZTD at any location relative to the reference location. In the next section, we use that model to compute the seasonal amplitude of the differenced ZTD for twenty-one GPS stations distributed over the island of Hawaii.

5 ZTD CORRECTION TO GPS DATA

The differenced seasonal ZTD signal at any location with respect to the reference station can be estimated either by fitting the sinusoidal signal to the DInSAR-derived height time-series (eq. 3) or computing the elevation-dependent amplitudes from eq. (9) and the frequency from the FFT analysis. Because the derived ZTDs are the values between the DInSAR points and a reference point, as discussed earlier, they can be used to remove the seasonal tropospheric delay in the differenced GPS position time-series relative to a reference station (Ge *et al.* 2003). Here we compare the modelled and observed seasonal amplitudes of the local ZTD at each GPS site relative to the reference station collocated with the DInSAR reference point.

In this paper, the daily RINEX files for each GPS station, at 15-s intervals, are processed based on the PPP processing strategy, which calculates the absolute position without attaching to a reference station. To do so, we use the online service from CSRS-PPP. The main advantage of the PPP approach is that, unlike differential processing approaches, the ZTD is considered an unknown parameter and therefore is estimated along with the position.

All the post-processed position solutions are in the International Terrestrial Reference Frame (ITRF2008) and are computed in the static mode using precise satellite orbits and clocks. One of the advantages of this service is that there is no minimum for a GPS observation session and the longer observation period makes it possible to resolve the carrier phase ambiguities required to recover more accurate positions (NRCan GSD 2004; Geng *et al.* 2012). In addition to using the antenna phase centre calibration value published by IGS, this service includes ocean loading corrections computed

Downloaded from https://academic.oup.com/gji/article-abstract/216/1/676/5144766 by CSIC user on 11 June 2020

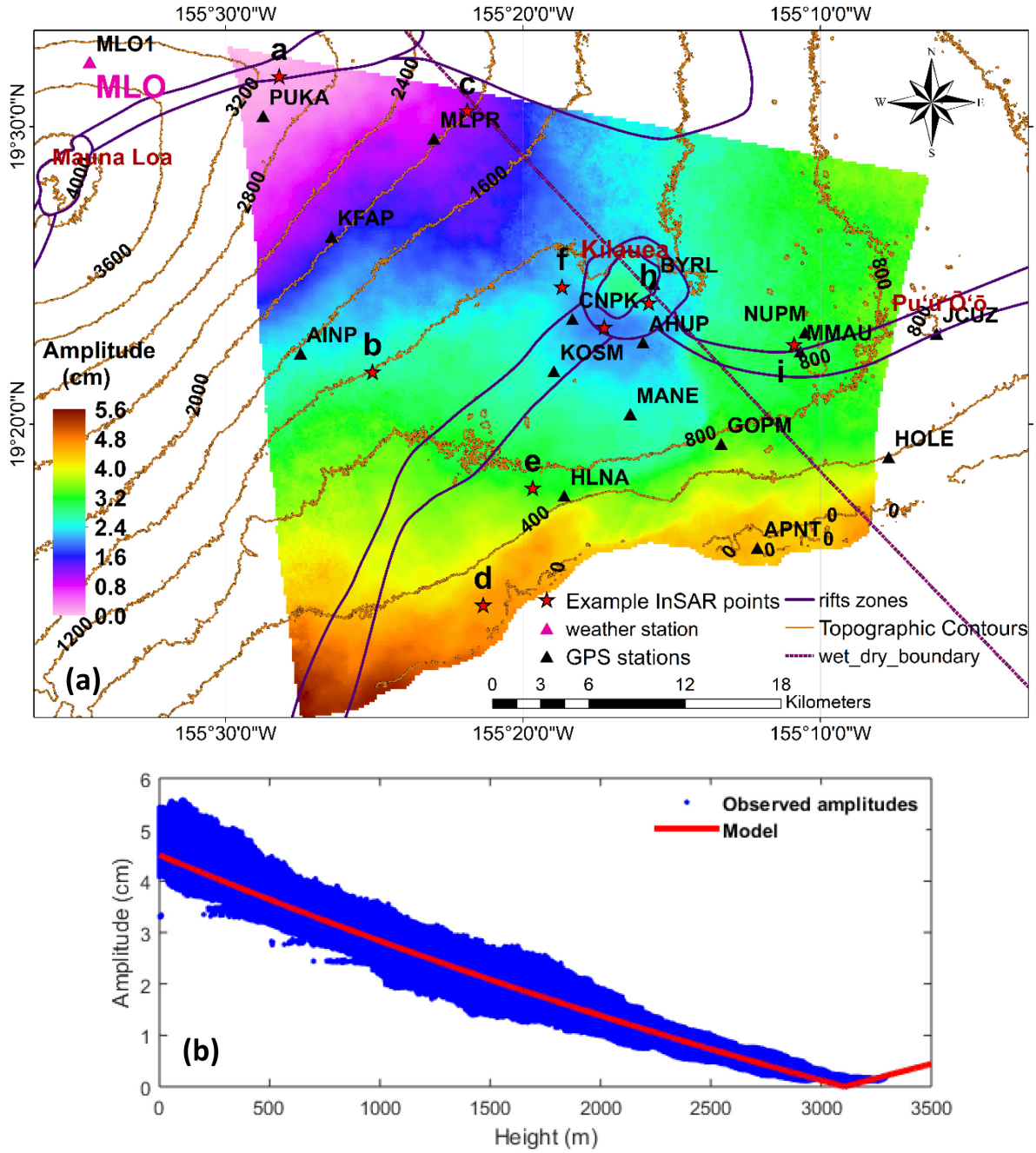

Figure 5. (a) Map of the measured amplitudes of seasonal variations of troposphere signal in DInSAR data by modelling a sinusoidal signal to the height time-series at each point. The brown contour lines represent elevations spaced at 400 m intervals. The rift zones of Mauna Loa and Kilauea are shown as dark lines. Separation between dry and wet regions are shown by the dashed line. (b) The vertical profile of the measured amplitudes as a function of height (blue) overlain with the modelled amplitudes by using eq. (9) (red).

with OSO Chalmers grid model (Bos & Scherneck 2011). This service also uses an ionospheric-free linear combination of L1 and L2 of the code and phase observations to eliminate the ionospheric delay.

CSRS-PPP estimates ZTD by employing the Global Mapping Function (GMF; Boehm et al. 2006a; Boehm *et al.* 2007). The minimum elevation angle of 10° is applied by default. This function is based upon the monthly average of pressure, temperature, and relative humidity data on a 1.5° × 1.5° global grid profile produced from the ECWMF numerical weather model (Kouba 2008), 40-yr re-analysis data (ERA40). This function is the spherical harmonic expansion of VMF1 (Boehm *et al.* 2006b) parameters and requires the station coordinates and day of the year as input parameters.

From the processing of the data of each GPS station by using CSRS-PPP, we obtain precise coordinates and ZTD, so called ZTD_{PPP}, with a time step of 15 s, for the period from 2014 to 2017. Because higher frequency fluctuations in the time-series are caused by fluctuations in the atmospheric parameters that cannot be attributed to the seasonal tropospheric variability, we compute the daily averaged time-series to better observe the seasonal variations. In this way, we select those dates which match the DInSAR observation dates. The differenced ZTD at each station, so called

Downloaded from https://academic.oup.com/gji/article-abstract/216/1/676/5144766 by CSIC user on 11 June 2020

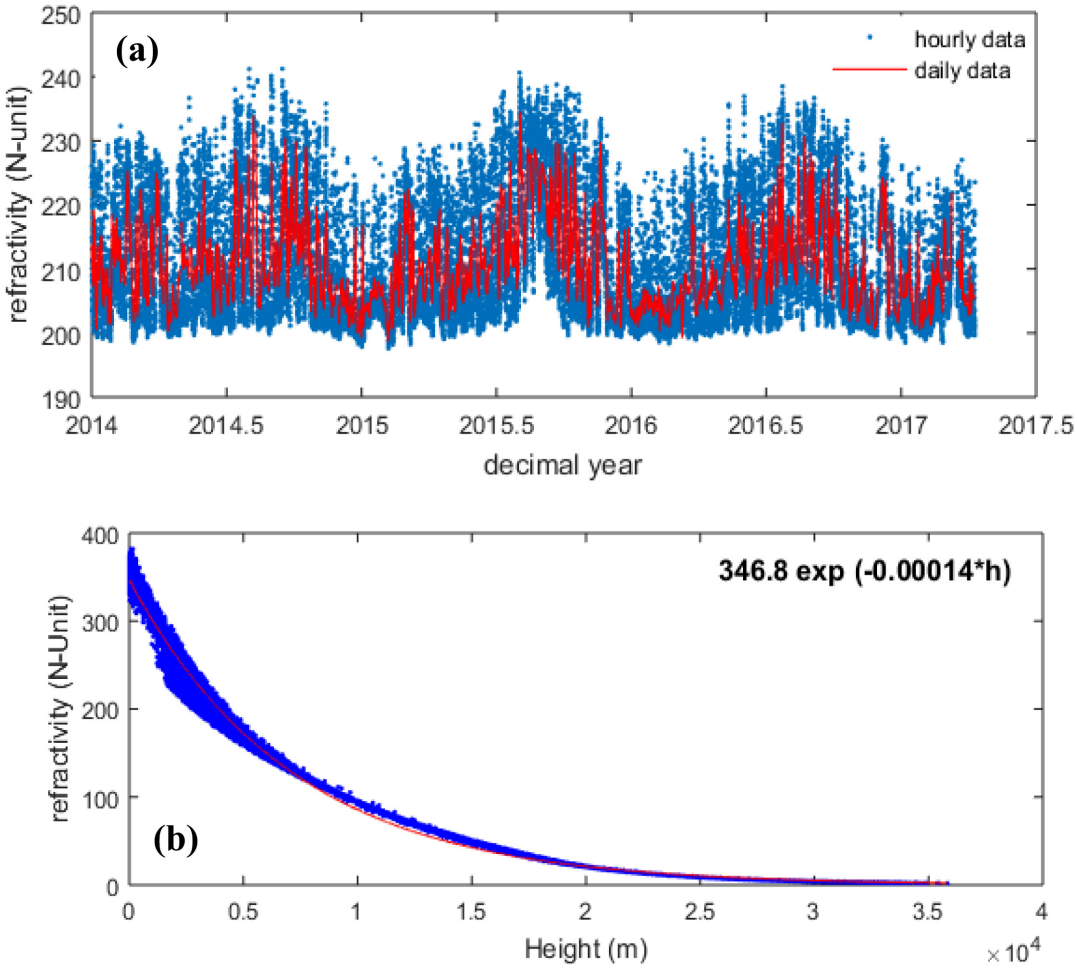

Figure 6. (a) The hourly time-series of the refractivity of atmosphere at the surface of Earth computed from the pressure, water vapour pressure and temperature time-series observed at the weather station MLO1 (in blue). The daily averaged refractivity time-series computed from hourly data (in red). (b) The vertical profile of the refractivity calculated from the meteorological parameters observed at the radiosonde station PHTO/HILO. The fitted red line is the best fit exponential function.

ΔZTD_{PPP}, is computed by subtracting the ZTD_{PPP} time-series estimated for station PUKA from those computed for the other GPS stations at the common dates (Fig. 7). Station PUKA at elevation 2999.8 m and a distance of 4.8 km from the DInSAR reference point is considered as the reference station, in order to maintain consistency in interpreting the results.

By analysing each ΔZTD_{PPP} in the frequency domain using an FFT approach, we identify the frequency of the seasonal variations, and then fit a Fourier series (eq. 3) to extract the phase and amplitude of the seasonal oscillations. These observed seasonal time-series in each ΔZTD_{PPP} are shown in Fig. 7. The maximum and minimum of the seasonal variations of ΔZTD_{PPP} occurs in the summer and in the winter, respectively. The observed seasonal amplitudes obtained by fitting the sinusoidal functions to each ΔZTD_{PPP} are presented in Table 3. This table also presents the seasonal amplitudes of the ΔZTD_{PPP} between 2014 and 2017. These are computed from eq. (9) by substituting the elevation of each GPS station above msl for z_i and the elevations of the reference point, 2999.8 m, for z_r. Fig. 7 also shows the seasonal signal produced with the modelled amplitude and the frequency obtained from the FFT for each station at the DInSAR acquisition dates (black star).

According to Table 3, the modelled amplitudes computed for each GPS station increases with the increase in the height difference from the reference station, as expected from the elevation-dependent exponential model, such that the estimated amplitude for station MLO1, at height 3402.7 m above msl, is greater than that estimated for station ALEP, at height 2895.7 m above msl. This model produces seasonal amplitudes of as much as 4 cm for stations APNT, PUH2 and HILR referenced to PUKA. These stations are located at the lowest altitudes and are close to the ocean. The lower seasonal amplitudes, less than 1 cm, are observed for stations located on Mauna Loa summit region, for example, TOUO, MLO1 and ALEP referenced to PUKA. The seasonal variations of atmospheric parameters at these stations are small compared to the variations at other stations.

Comparison between the observed and the modelled seasonal amplitudes shows that their differences for all ΔZTD_{PPP} s are in the range of $\pm$1.3 cm for all stations except for stations APNT, MMAU, and KFAP which are 2.3, 1.7 and -2.0 cm, respectively. As shown in Table 3, the computed rmse of the residuals between the modelled seasonal signals and ΔZTD_{PPP}, rmse-M in the table, ranges from 0.7 to 4.1 cm for stations ALEP and HILR relative to PUKA, respectively. As discussed by Jin *et al.* (2007), the unmodelled residuals

Downloaded from https://academic.oup.com/gji/article-abstract/216/1/676/5144766 by CSIC user on 11 June 2020

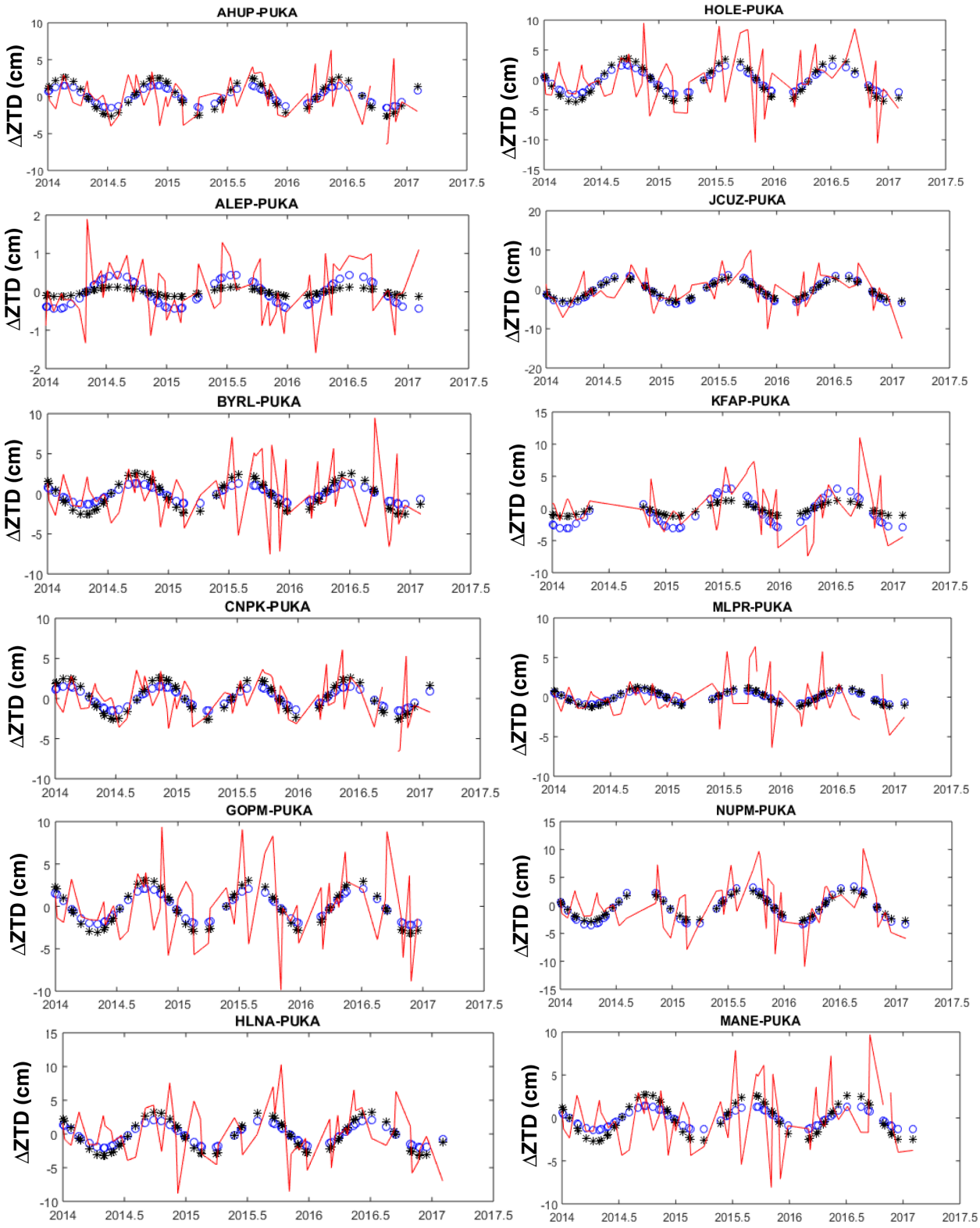

Figure 7. ΔZTD_{PPP} for each GPS station relative to the reference station, PUKA, shown in red overlain with the observed seasonal oscillations obtained from Fourier series analysis (blue circles). The modelled seasonal variation of ZTD estimated from eq. (9) is shown in black stars.

reflect the high-frequency variations (short period) in the wet component of tropospheric error and therefore change with altitude. We observe a maximum value of up to 4.1 cm, for the stations close to the coast and in the windward side of the island, HILR and HOLE, where the rainfall and relative humidity are high. The estimated rmse of the residuals for the modelled seasonal signal (Table 3) are in good agreement with those computed between the observed seasonal signals and ΔZTD_{PPP}, rmse-O in the table, and range from

Downloaded from https://academic.oup.com/gji/article-abstract/216/1/676/5144766 by CSIC user on 11 June 2020

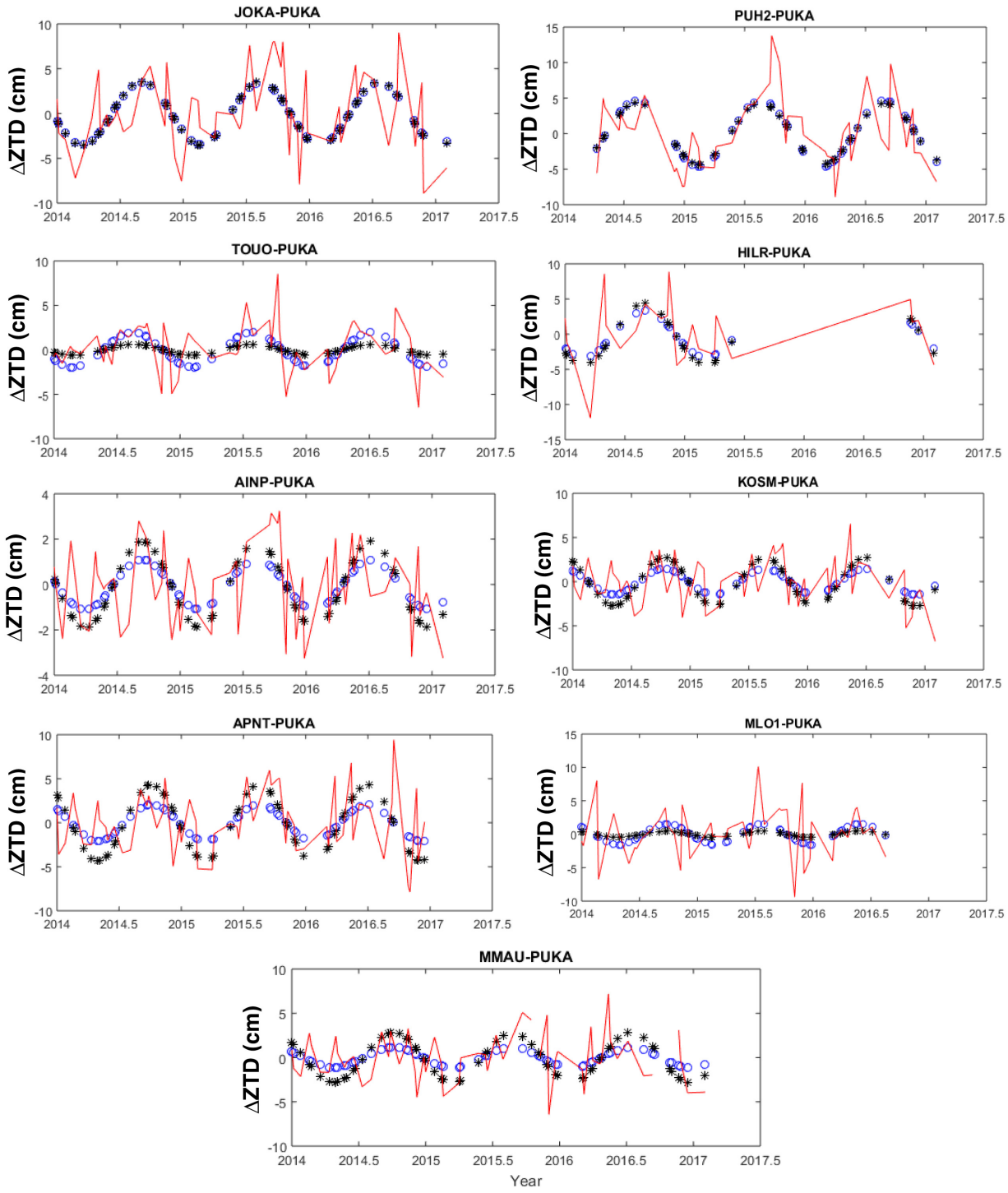

Figure 7. (*Continued.*)

zero to 0.3 cm. The greatest differences in the rmse of the residuals are 0.2–0.3 cm and are seen for stations TOUO, MMAU and APNT. Comparing the rmse of the residuals between the modelled and observed seasonal signals at every station indicates that the proposed model is able to predict the seasonal variation at every station with rmse values smaller than 1 cm, again with the exception of stations MMAU, APNT and KFAP. As stated earlier, the large differences in the observed and modelled seasonal amplitudes are seen for these three stations.

6 CONCLUSIONS

In this paper, we have taken advantage of the similarities of the effect of ZTD on both GPS and DInSAR data to model the local seasonal variations of ZTD on the GPS time-series relative to a reference station. We used DInSAR data with high spatial and temporal resolution to estimate the altitude-dependent ZTD correction in a region of high topographic relief, the area surrounding the Kilauea volcano in Hawaii, and applied that to the local GPS network time-series.

Downloaded from https://academic.oup.com/gji/article-abstract/216/1/676/5144766 by CSIC user on 11 June 2020

Table 3. Altitude of the GPS stations from Table 2.

Station	Altitude (m)	Length (km)	Period (yr)	Observed amplitude (cm)	Modelled amplitude (cm)	rmse-O (cm)	rmse-M (cm)	rmse (modelled and observed) (cm)
HILR	12.8	50.8	1.0	3.3	4.4	4.0	4.1	0.7
APNT	23.7	39.5	1.2	2.1	4.3	3.2	3.6	1.5
PUH2	29.4	46.0	1.0	4.6	4.3	3.6	3.6	0.2
HOLE	408.4	42.5	1.1	2.4	3.7	4.0	4.0	0.8
JOKA	466.5	50.5	1.1	3.4	3.6	3.6	3.6	0.1
HLNA	677.1	29.5	1.2	2.1	3.2	3.6	3.7	0.8
GOPM	739.4	33.8	1.2	2.1	3.1	3.9	3.9	0.7
JCUZ	808.8	41.9	1.0	3.6	3.0	3.6	3.7	0.4
NUPM	913.3	34.6	1.1	3.5	2.9	3.8	3.8	0.4
MMAU	929.7	34.8	1.1	1.1	2.8	2.5	2.7	1.1
KOSM	967.7	23.3	1.2	1.5	2.8	2.4	2.6	0.9
MANE	975.1	28.4	1.1	1.4	2.8	3.3	3.4	0.9
BYRL	1076.7	25.3	1.1	1.3	2.6	3.4	3.5	0.8
AHUP	1082.9	26.4	1.3	1.5	2.6	2.4	2.5	0.7
CNPK	1100.9	22.1	1.3	1.5	2.6	2.4	2.5	0.7
AINP	1543.1	14.9	1.1	1.1	1.9	1.6	1.7	0.5
MLPR	2015.9	10.1	1.1	0.9	1.2	2.4	2.4	0.2
KFAP	2048.0	8.5	1.0	3.1	1.2	3.5	3.5	1.3
TOUO	2509.6	23.5	1.1	1.9	0.6	2.3	2.5	0.9
ALEP	2895.7	17.8	1.0	0.4	0.1	0.6	0.7	0.2
PUKA	2999.8	0.0	0.0	—	—	—	—	—
MLO1	3402.7	10.8	1.2	1.6	0.5	3.5	3.5	0.8

Notes: Length is the distance between the reference station, PUKA, and each station. The period and the observed amplitude of the seasonal variations of ΔZTD_{PPP} obtained from Fourier series analysis are presented. The modelled amplitude is the seasonal amplitude between each station and PUKA estimated from eq. (9). The rmse-M is the rmse of the residuals between ΔZTD_{PPP} and the modelled seasonal component at each station. The rmse-O is the rmse of the residuals between ΔZTD_{PPP} and the observed seasonal signal in ΔZTD_{PPP} for every station. The rmse of the residuals between the modelled and the observed seasonal signals also are presented. Stations are sorted based on altitude.

In this research, DInSAR-derived height time-series obtained from the MSBAS processing of 66 SAR images from 2014 through 2017 were analysed to produce seasonal troposphere corrections. Motivated by Samsonov *et al.* (2014), we proposed an elevation-dependent exponential model from the meteorological data observed at the surface weather station close to the DInSAR reference point and radiosonde data, PHTO/HILO. The observed seasonal amplitudes in the height time-series range between 0.2 and 5.6 cm. This model provided the best fit to the vertical profile of more than 99 percent of the observed amplitudes. Based on this model, the magnitude of the seasonal amplitudes of the tropospheric delay in DInSAR data grow exponentially with increasing and decreasing elevation from the reference point at 3107 m above msl.

In order to evaluate the potential of the proposed model to predict the seasonal variations of local ZTD, the seasonal amplitudes observed in every differenced ZTD, ΔZTD_{PPP} (the difference between the ZTDs computed for each station and for the reference station, PUKA, obtained using CSRS-PPP application) were compared to the modelled seasonal amplitudes. We observed generally good agreement, in the range of ± 1.3 cm, between the modelled and the observed seasonal amplitudes for eighteen stations. The estimates of the rmse between the modelled and the observed seasonal signal for these stations ranges from zero to 0.9 cm. Comparing the rmse of the residuals between ΔZTD_{PPP} and the observed seasonal signals to those obtained between $\Delta ZTD_{PPP}$and the modelled seasonal signals also shows good agreement, with a maximum disagreement of 0.3 cm.

These results indicate that the proposed model using DInSAR data can accurately estimate the elevation-dependent seasonal amplitude of ZTD on a local scale. The main advantage of this model is that it eliminates the need for meteorological data at the location of each GPS station and it can be used in local networks in lieu of the low spatial resolution of numerical weather prediction models. Implementation of this methodology into GPS time-series processing is relatively simple and can be extended to virtually every region on Earth, particularly given the recent and upcoming increase in freely available DInSAR data, predominantly from the currently operational European Space Agency (ESA) Sentinel-1A/B C-band radar satellites and the NASA-ISRO Synthetic Aperture Radar (NISAR) L-band satellite, due to be launched in the next few years. ZTD corrections for local regions using images obtained from these satellites can model and estimate the tropospheric errors for the dominant frequencies and be incorporated as corrections into GPS time-series estimates. These corrections will only improve with the increased density of Sentinel-1A/B time-series, at acquisition intervals of 6–12 days. In addition, future research will include the combination and incorporation of both L-band and C-band estimates into this model and the potential improvements in our ability to estimate and remove the tropospheric errors in GPS observations. This research also could provide important contributions to in future studies of tropospheric variation in both space and time. Again, the use of a spatially dense local corrections, instead of the low resolution global weather prediction models, can improve the accuracy of positioning estimates at better spatial resolutions in future studies of GPS data in a variety of regions and natural hazards applications.

ACKNOWLEDGEMENTS

The authors would like to thank the Canadian Space Agency (CSA) for providing RADARSAT-2 data. We also thank NRCan for providing the CSRS-PPP online service accessible at https://webapp

Downloaded from https://academic.oup.com/gji/article-abstract/216/1/676/5144766 by CSIC user on 11 June 2020

.geod.nrcan.gc.ca/geod/tools-outils/ppp.php. We acknowledge Giambelluca et al. (2014) and the University of Hawaii for making the data and the raster maps of the climate variables freely available on http://climate.geography.hawaii.edu. Also, we appreciate University of Wyoming for providing the radiosonde data freely available on http://weather.uwyo.edu/upperair/sounding.html. Additionally, we thank the National Oceanic and Atmospheric Administration (NOAA) and Earth System Research Laboratory (ESRL) for making the meteorological data of in situ stations accessible at https://www.esrl.noaa.gov/. UNAVCO provided the direct FTP access to the GPS data on ftp://data-out.unavco.org/pub/rinex. Finally, we thank USGS for providing SRTM DEM at a resolution of 1 arc-second at https://earthexplorer.usgs.gov/. All data generated or analysed during this research can be obtained by contacting the authors. This research is supported by the NSERC Collaborative Research and Development (CRD) grant, 'Real-time ground motion tools for seismic hazard management'. The work of KFT was supported by an NSERC Discovery Grant.

REFERENCES

Alduchov, O.A. & Eskridge, R.E., 1996. Improved Magnus form approximation of saturation vapor pressure, *J. Appl. Meteorol.,* **35**(4), 601–609.

Baker, S. & Amelung, F., 2015. Pressurized magma reservoir within the east rift zone of Kīlauea Volcano, Hawai'i: evidence for relaxed stress changes from the 1975 Kalapana earthquake, *Geophys. Res. Lett.,* **42**.

Bean, B.R. & Dutton, E.J., 1968. *Radar Meteorology*. Dover Publications, Inc., New York.

Bean, B.R. & Thayer, G.D., 1959. Models of the atmospheric radio refractive index, *Proc. IRE,* **47,** 740–755.

Bevis, M., Businger, S., Chiswell, T., Herring, A., Anthes, R., Rocken, C. & Ware, R., 1994. GPS meteorology: mapping zenith wet delays on to precipitable water, *J. Appl. Meteorol.,* **33,** 379–386.

Bevis, M., Businger, S., Herring, T., Rocken, C., Anthes, R. & Ware, R., 1992. GPS meteorology: remote sensing of atmospheric water vapor using the Global Positioning System, *J. geophys. Res.,* **97**(D14), 15 787–15 801.

Boehm, J., Heinkelmann, R. & Schuh, H., 2007. A global model of pressure and temperature for geodetic applications, *J. Geod.,* **81**(10), 679–83.

Boehm, J., Niell, A., Tregoning, P. & Schuh, H., 2006a. Global Mapping Function (GMF): a new empirical mapping function based on numerical weather model data, *Geophys Res. Lett.,* **33,** L07304, doi:10.1029/2005GL025546.

Boehm, J., Werl, B. & Schuh, H., 2006b. Troposphere mapping functions for GPS and very long baseline interferometry from European Centre for Medium-Range Weather Forecasts operational analysis data, *J. geophys. Res.,* **111,** B02406.

Bos, M.S. & Scherneck, H.G., 2011. *Free Ocean Tide Loading Provider URL*http://holt.oso.chalmers.se/loading.

Clague, D.A. & Sherrod, D.R., 2014. Growth and degradation of Hawaiian volcanoes, in: *Characteristics of HawaiianVolcanoes,* pp. 97–146, Chapter 3, eds Poland, M.P., Takahashi, T.J. & Landowski, C.M., USGS Professional Paper 1801.

Colleen, D., 2013. Spatial Distribution of Freshwater Resources on the Hawaiian Island

Costantini, M., 1998. A novel phase unwrapping method based on network programming, *IEEE Geosci. Remote Sens.,* **36**(3), 813–821.

Dousa, J. & Vaclavovic, P., 2014. Real-time zenith tropospheric delays in support of numerical weather prediction applications, *Advances in Space Research,* Vol. **53,** 1347–1358, No 9, doi:10.1016/j.asr.2014.02.021.

Fiske, R.S. & Jackson, E.D., 1972. Orientation and growth of Hawaiian volcanic rifts: the effect of regional structure and gravitational stresses, *R. Soc. Proc.,* **329,** 299–326.

Flouzat, M., Bettinelli, P., Willis, P., Avouac, JP, Heriter, T. & Gautam, U., 2009. Investigating tropospheric effects and seasonal position variations in GPS and DORIS time series from the Nepal Himalaya, *Geophys. J. Int.,* **178**(3), 1246–1259.

Foster, J., Brooks, B., Cherubini, T., Shacat, C., Businger, S. & Werner, C.L., 2006. Mitigating atmospheric noise for InSAR using a high resolution weather model, *Geophys. Res. Lett.,* **33,** L16304, doi:10.1029/2006GL026781.

Fotiou, A. & Pikridas, C., 2012. *GPS and Geodetic Applications,* 2nd edn, Ziti.

Frazier, A., 2012. Month-year rainfall maps of the Hawaiian Islands, *M.A. thesis. University of Hawai'i at Manoa, M.A. thesis*, pp 81.

Gagné, W.C. & Cuddihy, L.W., 1990. Vegetation, In: *Manual of the Flowering Plants of Hawai'i,* pp. 45–114, eds Wagner, W.L., Herbst, D.R. & Sohmer, S.H., University of Hawai'i Press;/Bishop Museum Press.

Ge, L., Chang, H.C., Janssen, V. & Rizos, C., 2003. Integration of GPS, radar interferometry and GIS for ground deformation monitoring, *Proc. Int. Symp.,* on GPS/GNSS, Toyko, Japan, 15–18 November 2003. pp. 465–472.

Geng, J., Shi, C., Ge, M., Dodson, A.H., Lou, Y., Zhao, Q. & Liu, J., 2012. Improving the estimation of fractional-cycle biases for ambiguity resolution in precise point positioning, *J. Geod.,* **86**(8), 579–589.

Giambelluca, T.W. *et al.*, 2014. Evapotranspiration of Hawai'i. Final report submitted to the US Army Corps of Engineers—Honolulu District, and the Commission on Water Resource Management, State of Hawaii.

Goad, C.C. & Goodman, L., 1974. A modified Hopfield tropospheric refraction correction model, In *American Geophysical Union Annual Fall Meeting,* 12–17 December 1974, San Francisco, California, USA (abstract EOS Trans. AGU 55, 1106).

Goldstein, R.M. & Werner, C.R., 1998. interferogram filtering for geophysical applications, *Geophys Res. Lett.,* **25**(21), 4035–4038.

González, P.J., Tiampo, K.F., Camacho, A.G. & Fernandez, J., 2010. Shallow flank deformation at Cumbre Vieja volcano (Canary Islands): implications on the stability of steep-sided volcano flanks at oceanic islands, *Earth planet. Sci. Lett.,* **297**(3-4), 545–557.

Grell, A.G., Dudhia, J. & Stauffer, D.R., 1995. A description of the Fifth-Generation Penn State/NCAR Mesoscale model (MM5), In *NCAR Technical Note, NCAR/TN-398 STR*. National Center for Atmospheric Research, Boulder, CO.

Hanssen, R.F., 2001. *Radar Interferometry*. *Data Interpretation and Error Analysis*, Kluwer.

Hopfield, H.S., 1969. Two-quadratic tropospheric refractivity profile for correcting satellite data, *J. geophys. Res.,* **74,** 4487–4499.

Hopfield, H.S., 1972. Tropospheric range error parameters: further studies, in: *Applied Physics Laboratory Technical Memorandum TG1291,* Johns Hopkins Univ.

Jin, S., Park, J.U., Cho, J.H. & Park, P.H., 2007. Seasonal variability of GPS-derived zenith tropospheric delay (1994–2006) and climate implications, *J. geophys. Res.,* **112**(D9), doi:10.1029/2006JD007772.

Kouba, J., 2008. Implementation and testing of the gridded Vienna Mapping Function 1 (VMF1), *J. Geod.,* **82**(4), 193–205.

Kouba, J. & Heroux, P., 2001. *Precise Point Positioning Using IGS Orbit and Clock Products,* **5,** GPS Solutions, p. 12–28.

Lawrence, M.G., 2005. The relationship between relative humidity and the dewpoint temperature in moist air, *Bull. Am. Meteorol. Soc.,* **86,** 225–233.

Li, Z.H., Muller, J.P., Cross, P. & Fielding, E.J., 2005. Interferometric synthetic aperture radar (InSAR) atmospheric correction: GPS, Moderate Resolution Imaging Spectroradiometer (MODIS), and InSAR integration, *J. geophys. Res.,* **110**(2005)

Longman, R.J., Diaz, H.F. & Giambelluca, T.W., 2015. Sustained increases in lowertropospheric subsidence over the central tropical North Pacific drives adecline in high elevation rainfall in Hawai'i, *J. Clim.,* **28,** 8743–59.

Lu, C., Li, X., Li, Z., Heinkelmann, R., Nilsson, T., Dick, G., Ge, M. & Schuh, H., 2016. GNSS tropospheric gradients with high temporal resolution and their effect on precise positioning, *J. geophys. Res. Atmos.,***121,** 912–930.

Martin, F. & Waldron, C., 1961. A layered exponential model of radar refractivity, *J. geophys. Res.,* **66**(12), 4129–4135.

Mendes, V.B. & Langley, R.B., 1994. *A Comprehensive Analysis of Mapping Functions Used in Modeling Tropospheric Propagation Delay in*

Downloaded from https://academic.oup.com/gji/article-abstract/216/1/676/5144766 by CSIC user on 11 June 2020

Space Geodetic Data, International Symposium on Kinematic Systems in Geodesy, Geomatics and Navigations, Banff Canada.

NRCan GSD (Natural Resources Canada Geodetic Survey Division), 2004, On-line precise point positioning Project-How to use document, V.1.1, 2004.

Peterson, D.W. & Moore, R.B., 1987. *Geologic History and Evolution of Geologic Concepts, Island of Hawaii,* **vol. 1,** pp. 149–189, C hapter 7 ofeds Decker, R.W., Wright, T.L. & Stauffer, P.H., USGS Professional Paper 1350, Volcanism in Hawaii.

Poland, M., Miklius, A., Sutton, J. & Thornber, C., 2012. A mantle-driven surge in magma supply to Kīlauea Volcano during 2003–2007, *Nat. Geosci.,* **5,** 295–300

Rüeger, J., 2002. *Refractive index formulae for electronic distance measurements with radio and millimetre waves,* **109,** Unisurv Rep., Sydney, Australia., p. 758–766.

Saastamoinen, J., 1972. Atmospheric correction for the troposphere and stratosphere in radio ranging of satellites, in *The Use of Artificial Satellites for Geodesy, Geophys. Monogr,* voli. **15,** pp. 247–251, AGU.

Saastamoinen, J., 1973. *Contributions to the theory of atmospheric refraction Bullet. Geod.,* **107,** pp. 13–34.

Samsonov, S. & d'Oreye, N., 2012. Multidimensional time series analysis of ground deformation from multiple InSAR data sets applied to Virunga Volcanic Province, *Geophys. J. Int.,* **191**(3), 1095–1108.

Samsonov, S., Tiampo, K., Rundle, J. & Li, Z., 2007. Application of DinSAR-GPS optimization for derivation of Fine-Scale surface motion maps of Southern California, *IEEE Trans. Geosci. Remote Sens.,* **45**(2)

Samsonov, S.V. & d'Oreye, N., 2017. Multidimensional small baseline subset (MSBAS) for two-dimensional deformation analysis: case Study Mexico City, *Can. J. Remote Sens.,* doi:10.1080/07038992.2017.1344926.

Samsonov, S.V., Feng, W., Peltier, A., Geirsson, H., d'Oreye, N. & Tiampo, K.F., 2017. Multidimensional Small Baseline Subset (MSBAS) for volcano monitoring in two dimensions: opportunities and challenges. Case study Piton de la Fournaise volcano, *J. Volc. Geotherm. Res.,* **344,** 121–138.

Samsonov, S.V., Trishchenko, A.P., Tiampo, K., González, P.J., Zhang, Y. & Fernández, J., 2014. Removal of systematic seasonal atmospheric signal from interferometric synthetic aperture radar ground deformation time series, *Geophys. Res. Lett.,* **41,** 6123–6130.

Smith, E.F. & Gomberg, J., 2009. A search in strainmeter data for slow slip associated with triggered and ambient tremor near Parkfield, California, *J. geophys. Res.,* **114,** B00A14, doi:10.1029/2008JB006040.

Smith, E.K. & Weintraub, S., 1953. The constants in the equation for the atmospheric refractive index at radio frequencies, *Proc. IRE,* **41**(8), 1035–1037.

Spilker, J., 1996. Tropospheric effects on GPS, in: *Global Positioning System: Theory and Applications I,* **vol. 163,** pp. 517–546, eds Parkinson, B.W. & Spilker, J.J., American Institute of Aeronautics and Astronautics.

USGS (U.S. Geological Survey), 2017a. Hawaii Volcano Observatory, Volcano Hazards Program, visited July 07th, 2017.

USGS, 2017b. Hawaii Volcano Observatory, Active Volcanos of Hawaii, visited July 07th, 2017.

USGS, 2017c. Hawaii Volcano Observatory, Volcano Hazards Program, visited July 07th, 2017.

van Dam, T.M., Blewitt, G. & Heflin, M., 1994. Detection of atmospheric pressure loading using the Global Positioning System, *J. geophys. Res.,* **99,** 23 939–23 950.

Vedel, H., Mogensen, K.S. & Huang, X., 2001. Calculation of zenith delay from meteorological data: Comparison of NWP model, radiosondes and GPS delay, *Phys. Chem. Earth.,* **26,** 497–502.

Wadge, G. *et al.*, 2002. Atmospheric models, GPS and InSAR measurements of the tropospheric water vapour field over Mount Etna, *Geophys. Res. Lett.,* **29,** issn: 0094–8276, doi:10.1029/2002GL015159.

Wegmuller, U. & Werner, C., 1997. GAMMA SAR processor and interferometry software, in: *The 3rd ERS Symposium on Space at the Service of our Environment,* Florence, Italy.

Wilson, D., Elias, T., Orr, T., Patrick, M., Sutton, J. & Swanson, D., 2008. Small explosion from new vent at Kilauea's summit, *EOS, Trans. Am. geophys. Un.,* **89,** 203.

Yu, C., Penna, N.T. & Li, Z., 2017. Generation of real-time mode high-resolution water vapor fields from GPS observations, *J. geophys. Res.,* **122,** 2008–2025.

Zhang, C., Wang, Y., Hamilton, K. & Lauer, A., 2016. Dynamical downscaling of the climate for the Hawaiian Islands. Part II: Projection for the Late Twenty-First Century, *J. Cli.,* **29**(8), 3027–3048.

Downloaded from https://academic.oup.com/gji/article-abstract/216/1/676/5144766 by CSIC user on 11 June 2020